THE ASTROPHYSICAL JOURNAL, 426:294–307, 1994 May 1

HST ECLIPSE MAPPING OF DWARF NOVA OY CARINAE IN QUIESCENCE: AN "Fe II CURTAIN" WITH MACH ≃6 VELOCITY DISPERSION VEILS THE WHITE DWARF

KEITH HORNE,[1,2] T. R. MARSH,[3] F. H. CHENG,[1,4] IVAN HUBENY,[5] AND THIERRY LANZ[5]
Received 25 August 1993; accepted 1993 November 2

ABSTRACT

HST observations of the eclipsing dwarf nova OY Car in its quiescent state are used to isolate the ultraviolet spectrum (1150–2500 Å at 9.2 Å FWHM resolution) of the white dwarf, the accretion disk, and the bright spot. The white dwarf dominates the ultraviolet flux, with the disk and bright spot contributions increasing longward of 2000 Å. The white dwarf spectrum has a Stark-broadened photospheric Lα absorption, but is veiled by a forest of blended Fe II features that we attribute to absorption by intervening disk material. A fit gives $T_W \simeq 16.5 \times 10^3$ K for the white dwarf with a solar-abundance, log $g = 8$ model atmosphere, and $T \simeq 10^4$ K, $n_e \simeq 10^{13}$ cm^{-3}, $N_H \simeq 10^{22}$ cm^{-2}, and velocity dispersion $\Delta V \simeq 60$ km s^{-1} for the veil of homogeneous solar-abundance LTE gas. The veil parameters probably measure characteristic physical conditions in the quiescent accretion disk or its chromosphere. The large velocity dispersion is essential for a good fit; it lowers $\chi^2/778$ from 22 to 4. Keplerian shear can produce the velocity dispersion if the veiling gas is located at $R \simeq 5R_W$ with $\Delta R/R \sim 0.3$, but this model leaves an unobscured view to the upper hemisphere of the white dwarf, incompatible with absorptions that are up to 80% deep. The veiling gas may be in the upper atmosphere of the disk near its outer rim, but we then require supersonic (Mach ≃ 6) but sub-Keplerian ($\Delta V/V_{Kep} \simeq 0.07$) velocity disturbances in this region to produce both the observed radial velocity dispersion and vertical motions sufficient to elevate the gas to $z/R = \cos i = 0.12$. Such motions might be driven by the gas stream, since it may take several Kepler periods to reestablish the disk's vertical hydrostatic equilibrium. The temperature and column density of the gas we see as Fe II absorption in the ultraviolet are similar to what is required to produce the strong Balmer jump and line emissions seen in optical spectra of OY Car and similar quiescent dwarf novae.

The outer accretion disk is detected at mid-eclipse with a spectrum that rises from 0.05 to 0.3 mJy between 2000 and 2500 Å, consistent with combinations of cool blackbodies, blended Fe II emission lines, and Balmer continuum emission. The total disk flux density is 0.5 mJy at 2500 Å, and this shallow disk eclipse implies a roughly flat surface brightness distribution. The bright spot, somewhat bluer than the disk, has a flux density rising from 0.05 to 0.15 mJy between 1600 and 2500 Å. The C IV emission line has a broad shallow eclipse, but the radial velocity variations observed during the eclipse do not clearly distinguish between a disk or wind origin. The only possible indications of boundary layer emission are fast UV flares that appear to arise from near the central object—not from the bright spot.

Subject headings: accretion, accretion disks — binaries: eclipsing — novae, cataclysmic variables — stars: individual (OY Carinae) — white dwarfs

1. INTRODUCTION

Significant ultraviolet emission in cataclysmic variables may arise from the inner accretion disk, the boundary layer between the disk and the white dwarf, the photosphere of the white dwarf itself, and the bright spot where the gas stream from the companion star hits the outer rim of the disk. Novae, nova-like variables, and dwarf novae in outburst display blue ultraviolet spectra arising from a hot optically thick inner accretion disk, with broad emission lines (high-inclination systems) and P Cygni line structure (low-inclination systems) indicative of a wind emerging from this same region. In quiescent dwarf novae, the broad Lyman-alpha absorption lines seen in *IUE* spectra have been attributed to the photosphere of the white dwarf, and while this appears to be a plausible interpretation, there remains the concern that a hot optically thick inner accretion disk region is responsible for part or all of these Lα absorption line wings. The *Hubble Space Telescope* (*HST*) has high ultraviolet sensitivity and fast photon-counting spectrographs that make it possible to study eclipses of the ultraviolet light, providing new information about the spatial structure of the sources of ultraviolet radiation within the accretion flow.

In this paper we discuss time-resolved ultraviolet spectroscopy of an eclipse of the dwarf nova OY Car obtained with *HST*'s Faint Object Spectrograph (FOS). In § 2 we discuss the observations, present the ultraviolet eclipse light curves and spectra, and discuss the origin of the C IV emission. In § 3 we use the eclipse to decompose the data into white dwarf, bright spot, accretion disk, and flickering components. In § 4 we develop a fit to the observed white dwarf spectrum using a model atmosphere in local thermodynamic equilibrium (LTE)

[1] Space Telescope Science Institute, 3700 San Martin Drive, Baltimore, MD 21218. E-mail: cheng@stsci.edu
[2] Sterrekundig Instituut, University of Utrecht, Postbus 80 000, NL-3508 TA Utrecht, Netherlands. E-mail: horne@fys.ruu.nl
[3] Department of Astrophysics, University of Oxford, Keble Road, Oxford OX1 3RH, UK. E-mail: trm@astro.ox.ac.uk
[4] Center for Astrophysics, University of Science and Technology of China.
[5] Code 681, Goddard Space Flight Center, Greenbelt, MD 20771.
E-mail: hubeny@stars.gsfc.nasa.gov; lanz@stars.gsfc.nasa.gov

for solar abundance and log (g) = 8 observed through a veil of cooler solar abundance LTE gas that produces a forest of Fe II absorption features. In § 5 we discuss possible interpretations of the absorbing gas. Section 6 summarizes our principal findings.

2. *HST* OBSERVATIONS

2.1. *Instrumentation and Calibration*

We used the FOS with the Blue Digicon detector in its RAPID readout mode to obtain time-resolved ultraviolet spectra covering one eclipse of dwarf nova OY Car. OY Car was in the middle of a quiescent period between a normal outburst that started on August 28 and a superoutburst that started on 1992 April 7. A 39 m sequence of 234 spectra was obtained starting on UT 1991 December 4 at 8:45:17. The READ-TIME parameter was set to 10 s. This resulted in 8.166 s integrations separated by dead time gaps that varied in duration from about 1 to 1.5 s. The G160L grating covered 1154–2508 Å in first order. There is the possibility of contamination by the second-order spectrum beyond about 2400 Å, though we see no effects of this in the data. During data acquisition, the spectrum was shifted electronically by multiples of $\frac{1}{4}$ diode along the 516 diode Digicon array ("$\frac{1}{4}$ stepping"), resulting in a 2064 pixel spectrum sampled at 1.7 Å pixel^{-1} with a net exposure time of 2.04 s pixel^{-1}.

The spectral resolution for point sources derives from the spatial point spread function of the *HST* by first truncating it with the circular 1".0 diameter entrance aperture, then convolving with the intrinsic resolution of the spectrograph, and finally projecting onto the diode array. The resulting spectral resolution profile is well approximated by a Gaussian with a full width of 9.2 Å at half-maximum (Kinney 1992).

The undispersed order-zero reflection from the G160L grating is also recorded on the digicon array, providing a broad-band photometric measurement that is simultaneous with each of the ultraviolet spectra. We summed up the counts in pixels 501–750, and subtracted a background level derived from pixels 200–500 and 751–1050. The spectral bandpass of this order 0 light has been only crudely calibrated (Horne & Eracleous 1993). It has a broad response extending from 1150 to 5800 Å with a pivot wavelength of 3400 Å, a FWHM of 1900 Å, and a response of 820 counts per second for a 1 mJy source. We will refer to these as "white-light" measurements.

We have relied largely upon the standard data products from the FOS pipeline software. At the time of our observations, this software did not correct for an effect known as "GIMP," in which small wavelength and position shifts arise from geomagnetic deflections of the electronic signal beam within the spectrograph. These shifts of order 1 pixel on the blue side are too small to significantly affect our results. A small residual background due to particle hits on the detector and wide-angle scattering of the object's light within the FOS is also incompletely removed by the pipeline calibration. We improved upon the standard pipeline background calibration by using the substantial portions of the digicon detector that are not exposed to light when the G160L grating is used. The wavelength dependence of the pipeline background was scaled by a factor assumed to vary slowly in time to match the observed background level in the unilluminated parts of the detector. Finally, since we did not wish to spend half of our observing time measuring an off-target background spectrum, the geocoronal Lα emission has not been subtracted from our data, and it is found to be highly variable, decreasing by a factor of 4 during the 39 minute observation.

2.2. *Eclipse Light Curves*

Figure 1 shows the appearance of the eclipse as measured in a series of ultraviolet bandpasses, derived from the ultraviolet spectra, in comparison with the simultaneous white light curve.

The white light curve shown in Figure 1*a* displays distinctive eclipse features that are familiar from ground-based studies of OY Car and other eclipsing dwarf novae in quiescence. Sharp steps in the eclipse light curve represent the ingress and egress of the white dwarf and the bright spot behind the cool companion star. The white dwarf eclipse is (by definition) symmetric about binary phase 0, and its brightness is the same at ingress and egress.

The bright spot eclipse is delayed relative to phase 0 because the spot is located ahead of the line between the two stars, where the gas stream hits the outer rim of the disk. (Angular momentum carries the gas stream material forward as it falls from the inner Lagrangian point.) Note that OY Car appears brighter before eclipse than after, and that the bright spot is similarly brighter at ingress than at egress. The bright spot ingress is also slower than the egress. These features show that the bright spot is not a simple isotropic radiator. It may be

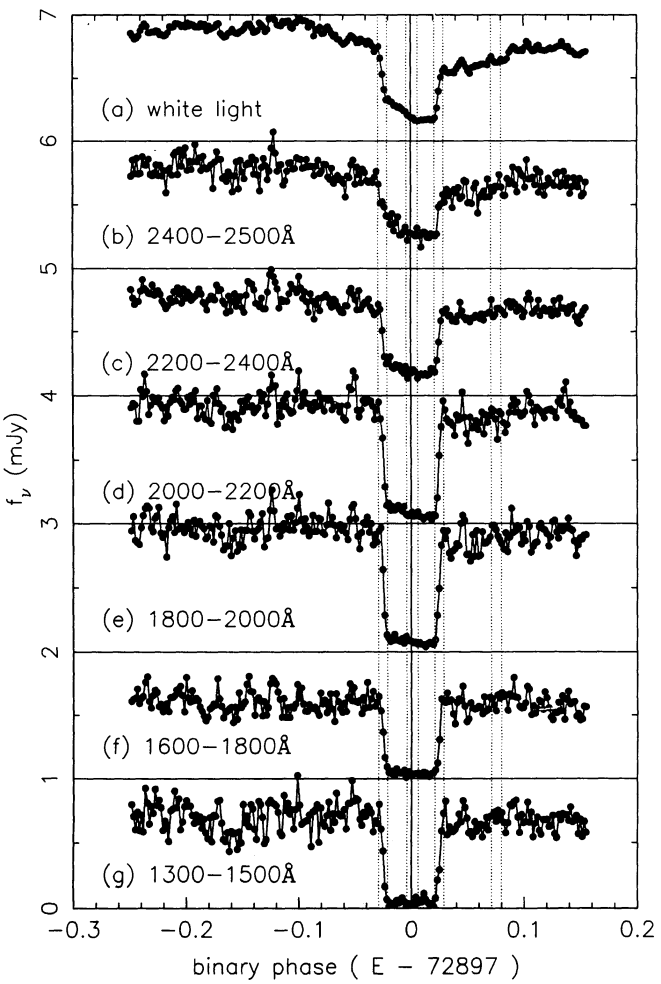

FIG. 1.—Eclipse light curves observed in white light and at various ultraviolet wavelengths obtained from the *HST*/FOS observations.

modeled as an extended or elongated region that is brighter before the eclipse, when it is viewed nearly face on, and fainter after the eclipse, when it is considerably foreshortened (Wood et al. 1989).

The white dwarf eclipse is centered on the heliocentric Julian date, corrected to Terrestial Dynamical Time (replacement for Ephemeris Time), HJED = 2,448,594.87873, which is about 40 seconds earlier than the prediction of the first ephemeris given in Wood et al. (1989). Therefore for the phases in this paper we retained the period of Wood et al.'s ephemeris but adjusted the constant term to give:

$$\mathrm{HJED} = 2443993.553411 + 0.0631209239E\ .$$

The white dwarf and bright spot contact phases that are marked in Figure 1 by vertical dashed lines are those from Wood et al. (1989), where a large number of eclipses observed in 1984 were averaged together to form a high quality mean light curve.

The ultraviolet eclipses in Figure 1 show that the white dwarf is an increasingly dominant component at shorter wavelengths. The eclipse at 1400 Å is particularly steep-sided and flat-bottomed, indicating that the white dwarf is the only significant source of radiation at this wavelength. A small residual flux at mid-eclipse may be attributed to background subtraction uncertainties mentioned above. The width of the white dwarf eclipse in the *HST* data is in good agreement with the contact phases from the ground-based study.

The bright spot contribution is evident at 1700 Å and longer wavelengths as a decreasing flux across the flat bottom of the eclipse, and a diminished flux after eclipse as compared with that before. Both features become more apparent at longer wavelengths. The bright spot ingress and egress features are not very sharply defined in comparison with their counterparts in the mean light curve of Wood et al. (1989). The ingress occurs earlier and the egress later in the *HST* data, indicating that the disk radius was slightly larger.

Light from the outer parts of the accretion disk is evident as a residual flux at mid eclipse, when the white dwarf and bright spot are both hidden behind the companion star. At wavelengths longer than about 2200 Å we also see a rising flux from phases $0.03 < \phi < 0.08$, which we may attribute to the egress of the disk because at these phases the white dwarf is fully visible and the bright spot is fully eclipsed.

2.3. *Spectra*

Figure 2 shows two ultraviolet spectra obtained by averaging data taken during out-of-eclipse phases ($|\phi| > 0.1$), when the white dwarf, disk, and bright spot are all visible, and during the eclipse phases ($|\phi| < 0.02$), when the white dwarf is occulted by the companion star. The white dwarf dominates the out-of-eclipse spectrum. The very irregular continuum level arises from a superposition of numerous strong absorption lines, mainly due to Fe II.

We have marked the expected positions of several Si and Al absorption features that are normally used for spectral classification of *IUE* spectra (Heck et al. 1984). These features are not clearly seen in the spectrum of OY Car. Analysis of the white dwarf spectrum is pursued in § 4. At mid-eclipse we see a smooth continuum rising longward of 2000 Å. This probably represents some combination of Balmer continuum emission, blended Fe II lines, and cool optically thick continuum radiation from the outer accretion disk, which is visible at mid-eclipse. The companion star is too cool to produce any significant continuum emission at 2000 Å.

Emission lines of Lα and C IV λ1549 are most prominent in the spectra. At mid-eclipse weaker emission lines become visible including C II λ1336, Si IV λ1400, Si II λ1816, Al III λ1855, Si III λ1892. Absent are the higher excitation lines He II λ1640

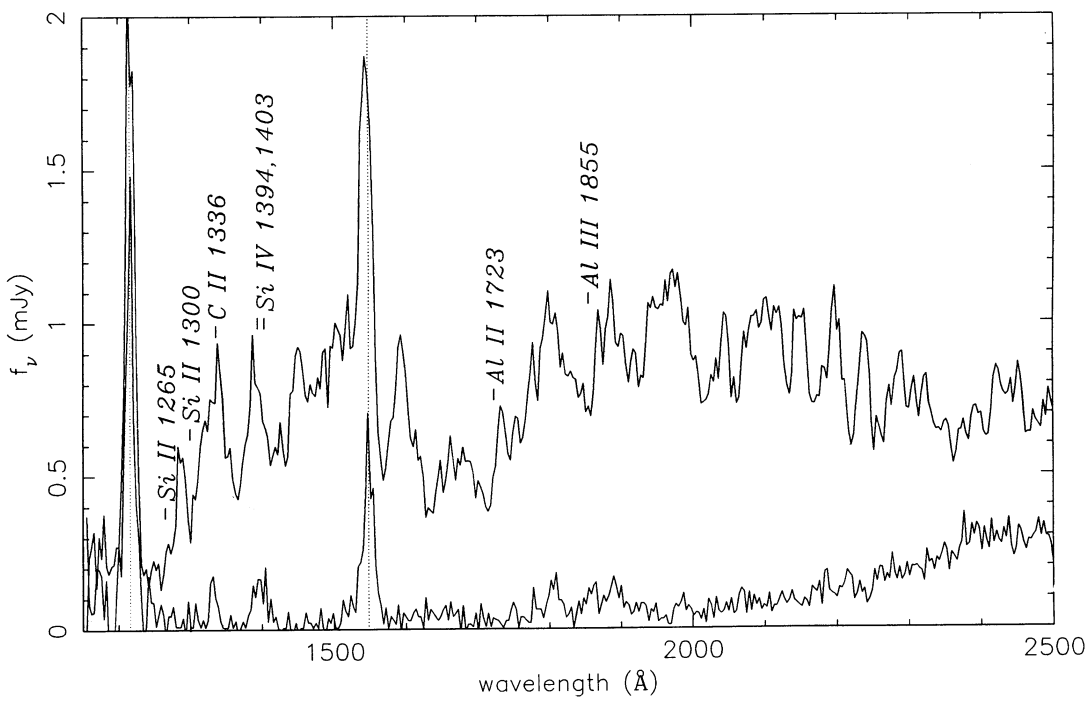

FIG. 2.—Ultraviolet spectra of OY Car obtained by averaging *HST*/FOS data from out-of-eclipse phases, and from phases in eclipse, when the white dwarf is occulted by the companion star.

and N v λ1240, and the semi-forbidden C III] λ1909. Note that there is no sign of emission around 2432 Å, where Lα emission would appear in second order, indicating that any contamination by the overlapping second-order spectrum must be weak.

2.4. *Emission Line Eclipses*

Figure 3 shows the light curve, radial velocity and full width at half-maximum (FWHM) of the Lα and C IV emission lines. We obtained these results by subtracting the white dwarf component derived from the light curve and spectrum decomposition discussed below, and then fitting Gaussian line profiles to the excess emission-line flux above a fitted continuum. The continuum subtraction was problematic for C IV because features in the white dwarf spectrum produce a strong slope across the profile.

The Lα emission is primarily geocoronal in origin. The Lα flux decreases by a factor of 4 in the first half of our observations, and then remains steady (Fig. 3*a*). There is no indication of an eclipse. The measured radial velocity is consistent with zero, and the 3400 km s^{-1} FWHM is consistent with expectations for a source that uniformly fills the 1".0 circular entrance aperture.

A broad partial eclipse is visible in the light curve of the C IV emission (Fig. 3*b*), indicating that C IV arises in an extended region larger than the size of the companion star. The line is significantly stronger before than after the eclipse, but our limited phase coverage does not allow us to determine whether this variation represents secular evolution or a phase-dependent anisotropy of the C IV emission. The measured FWHM of 3800 km s^{-1} is well above the instrumental resolution, which is 1800 km s^{-1} at 1550 Å for a point source centered in the 1".0 circular aperture. The FWZI is at least 6000 km s^{-1} but we cannot measure it very accurately due to the difficulty in removing the white dwarf spectrum. The radial velocity curve (measured relative to $\lambda = 1549.48$, the mean C IV doublet wavelength) shows a (3 σ) gradient from -800 km s^{-1} at phase -0.2 to -400 km s^{-1} at phase $+0.15$. The zero-point of this velocity scale is uncertain because the binary search onboard target acquisition procedure may have left the object somewhat mis-centered in the spectrograph aperture.

The observed C IV emission might arise from magnetic activity on the surface of the quiescent disk (Horne & Saar 1991), or from resonant scattering in a wind extending vertically well above the disk. While strong evidence for extended winds is found in the C IV line of systems with high mass accretion rates, such winds are not generally recognized to be important at the lower mass accretion rates typical of dwarf novae in quiescence. The C IV eclipse width in Figure 3*b* is similar to that of the disk, but a partial eclipse of an extended wind could produce a similar eclipse profile. If real, the blueshifted radial velocity could be more easily attributed to wind emission, since the inclined disk hides a larger fraction of material moving away from than toward the observer. A definitive signature of

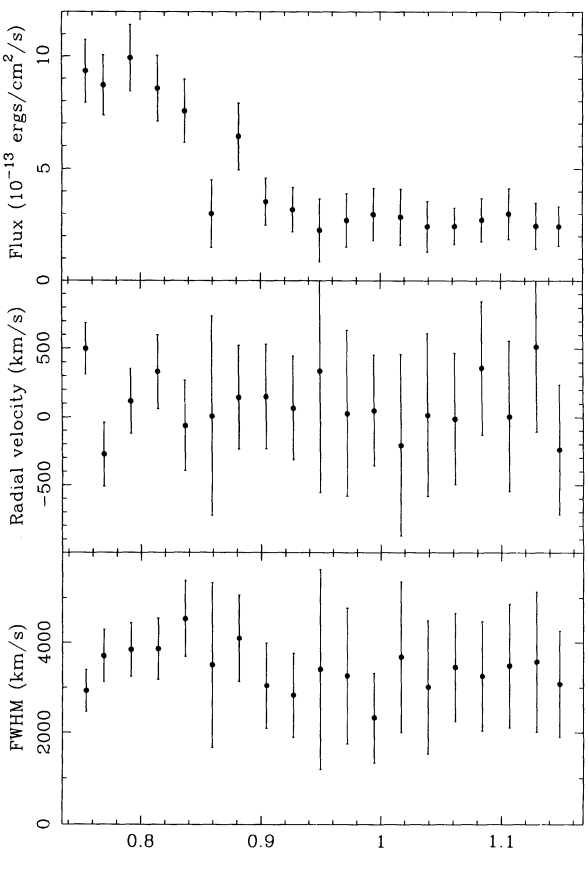

FIG. 3*a*

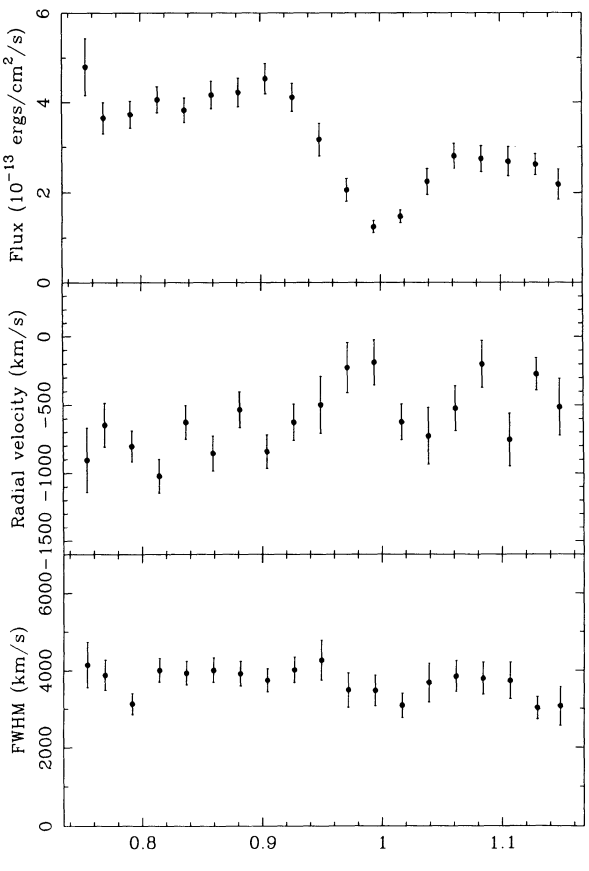

FIG. 3*b*

FIG. 3.—Fluxes, radial velocity, and full width at half-maximum curves for the Lα (*a*) and C IV (*b*) emission lines, obtained by fitting a Gaussian line profile after subtracting the white dwarf spectrum and a residual continuum from the spectra. The Lα emission is highly variable geocoronal emission showing no eclipse. C IV's blueshift and broad shallow eclipse suggest wind emission.

disk emission would be a rotational distortion (redshift then blueshift) during the eclipse, while wind emission should become redshifted as approaching material is covered during the eclipse. It is not clear which if either of these signatures is present. Thus we cannot clearly distinguish between disk and wind emission on the basis of the present data.

3. DISSECTING THE LIGHT CURVES AND SPECTRA

Distinctive features in the eclipse allow us to isolate the light curves and ultraviolet spectra of the white dwarf, the bright spot, and the accretion disk. The main results of this decomposition are highlighted in Figure 4, which shows the light curves, and Figure 5, which shows the spectra of these components. The residuals shown in Figure 4 reveal the presence of a flickering component. In the following subsections we discuss these results.

3.1. *Light Curve Decomposition*

We assume that the data $D(\phi, \lambda)$ can be modeled as a sum of several components each with separable time and wavelength dependences:

$$M(\phi, \lambda) = \sum_{i=1}^{N} L_i(\phi) S_i(\lambda) , \quad (1)$$

where $L_i(\phi)$ is the light curve and $S_i(\lambda)$ is the spectrum of component number i. The component light curves and spectra are adjusted as parameters of the model in order to achieve a best-fit to the data, as measured by the χ^2 statistic.

As a first step, we used the white light curve to define the shapes of the light curves of three components, the white dwarf, the bright spot, and the disk. Figure 4 shows the three-component light curves obtained for one particular fit to the data, as well as fits obtained by scaling the same light curve

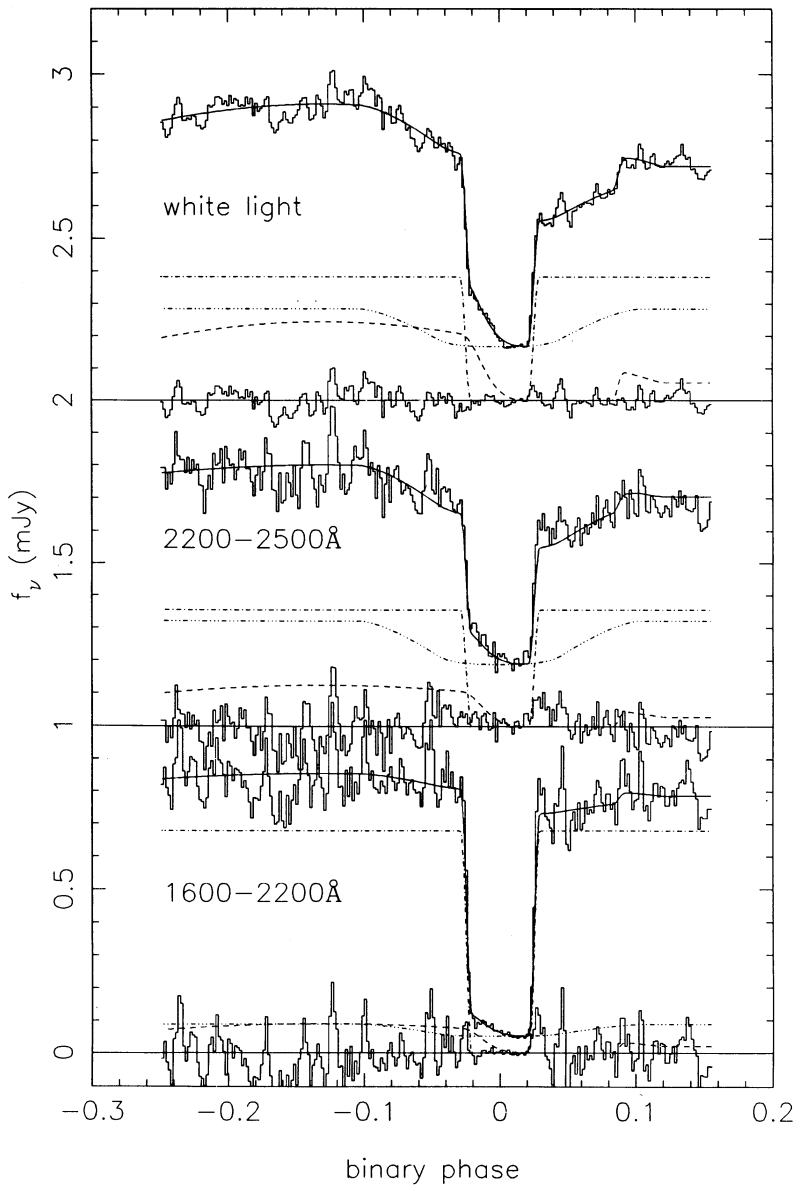

FIG. 4.—Decomposition of eclipse light curves into separate contributions from the white dwarf, bright spot, and accretion disk components. Fig. 4*a* shows a fit to the eclipse light curve observed in white light, from which the shapes of the three component light curves are determined. Figs. 4*b* and 4*c* show fits to ultraviolet curves binned from 2200–2500 Å and 1600–2200 Å, respectively, which hold fixed the shapes of the light curves but vary the fluxes of the three components.

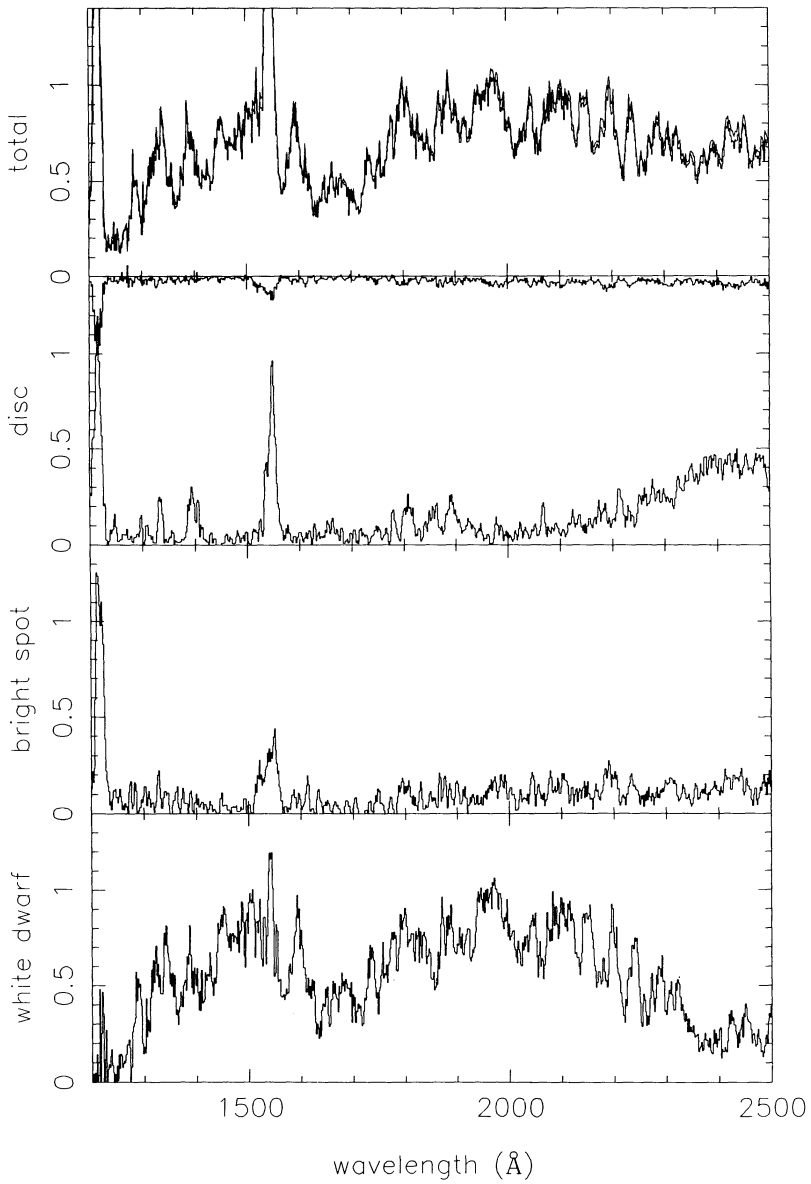

FIG. 5.—Spectra obtained for the white dwarf, bright spot, and disk components by scaling the component light curves (e.g., from Fig. 4) to fit the observed light curve at each ultraviolet wavelength. The upper panel shows the model, observed data, and residuals for the mean out-of-eclipse spectrum.

shapes to fit the ultraviolet data binned from 1600–2200 Å, where the white dwarf dominates, and from 2200–2500 Å, where the disk contributes.

Having settled upon the shapes of the component light curves, we next find the corresponding spectra by fitting the light curve observed at each ultraviolet wavelength using a linear combination of the three component light curves. Figure 5 shows the spectra that we found from such a series of linear regression fits. We will discuss the spectra presently, but let us first consider how we arrived at the light curves.

We used two different methods to define the component light curves, both of which gave similar results. The first method we tried followed a procedure similar to the light curve decomposition technique first described by Wood, Irwin, & Pringle (1985), and applied by Wood et al. (1989) to optical light curves of OY Car eclipses. While this decomposition is not unique, we were able to obtain plausible and fairly well determined light curves from the white-light eclipse data by imposing constraints on the various component light curves. For example, we assume that the white dwarf and disk light curves are symmetric about phase 0. Since the white dwarf and bright spot are totally eclipsed, their light curves must have a flux of 0 between their respective second and third contact phases. Outside their first and fourth contacts, the white dwarf and disk are assumed to be constant, while the bright spot is allowed to vary in a smooth way. We adjusted the contact phases to match the sharp features in the spectrum, though the bright spot ingress presented some difficulties as it is not very sharply defined in our data.

3.2. *A Parameterized Model of the Eclipse*

In our second and preferred approach, we developed a simple physical model of the binary system and used this model to compute eclipse light curves for the white dwarf,

bright spot, and disk components. This model assumes that the eclipses are due to occultations by the companion star, which exactly fills its Roche lobe. We adopt the inclination angle $i = 83.3$ and mass ratio $q = 0.102$ from the study of Wood et al. (1989). More specific details of the model are given in following subsections.

The parameters of the model were adjusted to fit the observed light curves in the following way: We started with initial values of 10 nonlinear parameters that control the shapes of the three light curves. A linear regression was used to scale the three light curves to fit the observed light curves in white light and at each ultraviolet wavelength. This gave estimates for the spectra of the three components. We then used the Amoeba algorithm (downhill simplex; Press et al. 1986) to adjust selected nonlinear parameters to find the best fit. The linear regression fits at individual ultraviolet wavelengths were often quite noisy, and gave strongly correlated estimates of the fluxes of the three components. To improve this situation, we imposed a positivity constraint—whenever a negative flux was found for one of the components, we set the flux of that component to zero and repeated the fit to solve for the fluxes of the other two. As a final step, we applied a 3 pixel boxcar smoothing to the final bright spot and accretion disk spectra, and then repeated the fit of the white dwarf spectrum.

The light curves shown in Figure 4 and spectra in Figure 5 are the final result of this fitting procedure. The main results of the fitting are summarized in Table 1, which gives the parameters of several best-fit models, and the corresponding goodness-of-fit statistics.

To quantify the goodness-of-fit between the model's predicted light curve and the observed data, we employ the χ^2 statistic. However, rather than assigning a priori error bars to the data points, we instead use

$$\sigma(\phi, \lambda) = \sqrt{Q(\lambda)M(\phi, \lambda)}\,, \qquad (2)$$

where $Q(\lambda)$ is the ratio of flux to counts, which is known from the FOS calibration, and $M(\phi, \lambda)$ is the model's predicted flux. This is necessary for our low count-rate data to approximate the Poisson statistics (ignoring the small background correction.) We note that the FOS pipeline software used $\sqrt{\max(1, N)}$ for the error bar on N observed counts, and this leads to unacceptable overestimates of the error bars at the low count rates in our time-resolved data.

3.3. *The White Dwarf*

We model the white dwarf as an unobscured spherical object with total flux F_W, radius R_W, and intensity distribution specified by a linear limb-darkening law with coefficient U_W. We compute the shape of the white dwarf eclipse using a fast three-point approximation for the limb of the Roche lobe (Wood & Horne 1990). Because the 9.5 s time resolution does not adequately resolve the rapid ingress and egress of the white dwarf, during these phases we evaluate the model light curve at closely spaced phases and compute the predicted flux by averaging over the phase range covered by each exposure.

From the light curve fits we see that the white dwarf flux F_W is fairly tightly constrained by the sharp jumps in the eclipse. Table 1 reveals a correlation between F_W and the radial intensity distribution in the disk. When we allow R_W to be a free parameter, with limb darkening fixed at $U_W = 0.5$, we find $R_W/R_{L1} = 0.0236$. This is close to the value found by Wood & Horne (1990), $R_W/R_{L1} = 0.0221$ (the average of their two values for $U_W = 0$ and 1). The difference may be attributed to uncertainty in our measurement due to flickering—we observed only one eclipse.

With the present data we did not consider it worthwhile to use the shape of the white dwarf ingress and egress to constrain parameters of a boundary layer. In later observations we have been able to obtain a somewhat higher time resolution, and we may be able to address this question in a future paper.

3.4. *The Quiescent Accretion Disk*

For the disk we use a series of concentric annuli in the orbital plane, and a power law for the radial intensity distribution extending from the inner disk radius $R_{in} = R_W$ to the outer disk radius R_D. The power-law index is b and the disk flux is F_D.

The disk component is constrained by the flux remaining at mid-eclipse, and by the slope of the light curve between the white dwarf egress and the bright spot egress. The slowly rising flux just before and after the white dwarf egress shows that the intensity of the white dwarf is more than 30 times larger than that of the inner disk. The best fit is for a nearly flat intensity distribution on the disk, with $b = +0.2 \pm 0.5$. Under such circumstances the geometry of the disk's partial eclipse in OY Car gives rise to a fairly broad and shallow eclipse light curve (e.g., Fig. 4). For $b > 1$ the disk eclipse is actually deepest at two

TABLE 1

WHITE LIGHT ECLIPSE PARAMETERS

	Model					
Parameter	Best-Fit	$b = -1$	$b = 0$	$b = 1$	$b = 2$	$b = 3$
q	0.102	0.102	0.102	0.102	0.102	0.102
i	83.3	83.3	83.3	83.3	83.3	83.3
F_W	0.384	0.320	0.375	0.403	0.417	0.426
R_W/R_{L1}	0.0236	0.0203	0.0231	0.0244	0.0251	0.0254
U_W	0.5	0.5	0.5	0.5	0.5	0.5
F_D	0.282	0.337	0.289	0.264	0.249	0.240
R_D/R_{L1}	0.602	0.588	0.602	0.603	0.603	0.602
b	0.23	−1	0	1	2	3
F_B	0.244	0.250	0.244	0.243	0.243	0.244
f_{iso}	0.234	0.257	0.228	0.228	0.225	0.228
θ_B	136.7	137.2	136.6	136.8	136.8	137.0
S/R_{L1}	0.044	0.067	0.045	0.041	0.040	0.040
χ^2/ν	7.11	7.54	7.09	7.14	7.31	7.50
ν	228	229	229	229	229	229

phases on either side of phase 0. Reasonable fits are possible while varying the disk's power-law index b from -1 through $+3$. The smaller values of b produce a deeper disk eclipse, and the fit responds by increasing the disk flux F_D and correspondingly decreasing the white dwarf flux F_W. Thus the outer disk flux is well determined by the observations at mid-eclipse, while the total disk flux is constrained mainly by the observations around phase 0.08 to an accuracy of about 10%.

3.5. *The Bright Spot*

For the bright spot we found that we needed a fairly complicated model. We used a linear strip passing directly through the point at which the gas stream trajectory crosses the outer disk radius R_D, with a radiating surface that is orthogonal to the orbital plane.

We tip the strip by an angle θ_B, measured relative to the direction from the white dwarf to the secondary star, to allow adjustment of the phase of the orbital hump. The intensity distribution along the strip is given by $(X/S)^2 e^{-X/S}$, where X is distance along the strip, and S defines the scale length of the bright spot's exponential tail, and hence the width of the bright spot ingress feature in the light curve. The maximum intensity along the strip, which occurs at $X = 2S$, is placed at the center of the stream trajectory. The total flux of the bright spot is F_B. We allow a fraction f_{iso} of this flux to be radiated isotropically, and the complementary fraction $(1 - f_{iso})$ to be radiated anisotropically, assuming foreshortening but no limb darkening.

The bright spot parameters are constrained by several aspects of the light curve. The phase of the egress feature defines the disk radius $R_D = 0.602 R_{L1}$, rather larger than that found by Wood et al. (1989). The difference in flux before and after the eclipse constrains the flux of the anisotropic component, while the size of the jump at bright spot egress defines the flux of the isotropic component. The phase of maximum brightness defines the orientation of the bright spot $\theta_B \simeq 137°$, roughly halfway between the flow directions of the disk rim (108°) and the stream (156°). The gradually declining flux seen just after white dwarf ingress determines the exponential scale length $S \simeq 0.04 R_{L1}$. The bright spot ingress is rather more gradual here than in the Wood et al. (1989) study.

3.6. *The Flickering Component*

There are about a dozen fast flares in the data, each lasting about 1 minute. From the residuals to the light curve fits in Figure 4, the flares seem to be well correlated at all wavelengths, with a larger amplitude and possibly a shorter timescale at shorter wavelengths. The flares are distributed fairly uniformly in phase, except that no flares are seen when the white dwarf is eclipsed. There may be a flare in progress at the time of white dwarf egress, and one flare at phase 0.04 occurs when the bright spot is totally eclipsed. Thus the phase distribution of the flares rules out the bright spot, and implicates the inner disk or white dwarf as the source of the flares.

Is this flickering in the inner disk/boundary layer of OY Car, or some instrumental modulation of the count rate due for example to spacecraft jitter? Although flares were not seen during the eclipse of the white dwarf, the flux is much lower then, so that we could not rule out the presence of flares with a fractional amplitude similar to those seen out of eclipse. We obtained a record of the spacecraft jitter during our observations and found no indication of tracking problems which might have caused the flares. We therefore believe that they are intrinsic to OY Car, and may represent stochastic time variability in the accretion process in the inner disk/boundary layer region.

4. MODELING THE WHITE DWARF SPECTRUM

The atmosphere of OY Car's white dwarf may be expected to differ considerably from those of single white dwarfs. The strong gravity at the surface of a white dwarf drives a sedimentation process that competes with thermal diffusion. At sufficiently low temperatures sedimentation wins, leading to an "onion skin" structure, with a layer of nearly pure (metal-free) hydrogen atop a layer of nearly pure helium atop layers of progressively heavier elements. Because the heavy elements sink down below the photosphere, they fail to leave their mark in the spectrum. Thus white dwarf spectra can to good approximation be modeled as pure hydrogen (DA type) or pure helium (DB type) atmospheres, with only traces of heavy element contamination.

OY Car's white dwarf may acquire a mixed-composition atmosphere through accretion from the disk. Heavy elements may also be dredged up from below the photosphere by turbulent mixing driven by the shear boundary layer on the equator of the white dwarf. The equilibrium reached between accretion, dredge-up, and settling may lead to surface compositions somewhere in the mixing space between the composition of the accreted material, that of the transition region/core of the white dwarf, and pure hydrogen. The determination of element abundances by analysis of the white dwarf's ultraviolet spectrum could therefore have interesting consequences.

4.1. *The Model Atmospheres*

In order to interpret the ultraviolet spectrum of the white dwarf in OY Car, we first computed a small grid of plane-parallel, hydrostatic model atmospheres (10,000 K $< T_{eff} <$ 20,000 K), $\log g = 8$. Models were calculated using computer program TLUSTY (Hubeny 1988), upgraded recently to incorporate the so-called accelerated complete linearization (Hubeny & Lanz 1992). All models were calculated relaxing the assumption of LTE, but in the studied range of the parameter space (particularly a large surface gravity), departures from LTE are generally quite small.

We assume solar composition. However, since we did not consider the effect of numerous metal lines on the atmospheric structure (line blanketing)—this effect is taken into account only for calculating synthetic spectra—we consider hydrogen, helium, and carbon, which are the dominant continuum opacity sources. The number of explicit NLTE energy levels for these elements is 8, 14, and 5, respectively. All hydrogen lines between the lowest eight levels are taken into account explicitly, using the NLTE occupation probability formalism (Hubeny, Hummer, & Lanz 1994).

The neglect of metal line blanketing is permissible for the present exploratory study, but for future studies, line blanketing must certainly be taken into account. Recently, we took a first step in this direction, and calculated several NLTE line blanketed model atmosphere for $T_{eff} = 15{,}000$ K and $\log g = 8$, and with varying metallicity (Lanz et al. 1992). Since the NLTE effects are negligible, the most important effect of line blanketing is a systematic shift in the effective temperature by a few hundred degrees at a given spectral type. In this study, we do not aim at determining an accurate effective temperature of the white dwarf; therefore the neglect of line blanketing in computing the model atmosphere (the temperature and density structure) is a reasonable approximation.

Once the model atmosphere grid is constructed, we calculate synthetic spectra using a separate program SYNSPEC (Hubeny 1994). Source functions for the resonance lines of the first twenty elements are calculated using the second-order escape probability theory (Hummer & Rybicki 1982), and the LTE source function is assumed for all other metal lines. The intrinsic line profiles are given by a Voigt function, with a damping parameter containing contributions of natural, Stark, van der Waals, and thermal Doppler broadening. The *gf*-values and the broadening parameters are taken from Kurucz's (1990) line list. The spectrum is calculated initially on a very fine wavelength grid (with a resolution of the order of 0.01–0.02 Å), and then convolved with a Gaussian (FWHM = 9.2 Å) to simulate the FOS spectral resolution.

4.2. *Bare White Dwarf Models*

When we first encountered the *HST* spectrum of OY Car's white dwarf, with its host of absorption line features, we became quite excited at the prospect of using them to measure surface abundances and the rotation and orbit velocities of the white dwarf. We spent some considerable time attempting to fit the observed spectrum with a bare white dwarf model by varying the temperature T_W and surface abundances, but without success.

Figure 6 shows models for several compositions fitted to the optical photometry of the white dwarf, which includes *B*, *V*, *R* fluxes from the eclipse study of Schoembs, Dreier, & Barwig (1987), and *U*, *B*, *R* photometry from Wood et al. (1989). The models shown in Figure 6 and those summarized in Table 2 are fitted to the optical photometric data only. These fits give a well-determined temperature of about 15,000 K, and a distance of about 92 pc (assuming $R_W = 0.011\ R_\odot$). The Balmer jump in absorption and Paschen continuum slope as defined by the broad-band photometry are well fitted by the model atmospheres. The temperature and distance are practically independent of composition, so long as hydrogen provides the main continuum opacity, since metal line blanketing is relatively weak in the optical.

However, the bare white dwarf models we have tried all fail to fit the *HST* spectrum, which has much deeper absorption features due mainly to blended Fe II lines. The pure hydrogen model in Figure 6*a* produces far more ultraviolet flux than observed. The solar composition model shown in Figure 6*b* has deeper but still insufficient line blanketing in the ultraviolet. Moreover, the pattern of absorptions is not similar to what we observe in OY Car. We tried several models with plausible nonsolar compositions, thinking that the accreted material might be some mixture of solar abundance material from the envelope and processed material from the core of the companion star. For example if nuclear burning proceeds primarily by the CNO cycle, the H nuclei are converted to He while C and O nuclei are converted to N. The decreased H lowers the continuum opacity and could thereby increase the equivalent widths of the metallic absorption features. But none of these models gave a pattern of absorption features resembling those in the *HST* spectrum of OY Car. We tried increasing and decreasing the gravity, but this had only minor effects on the relative line strengths. We tried increasing all metal abundances relative to hydrogen, holding the metal abundance ratios fixed at solar values. While the resulting spectra show Fe II features similar to those in the data, such features as Al III λ1855 were much stronger in the models than in the data.

The best fits we achieved were obtained by simply increasing the Fe abundance, holding other abundances fixed at solar values. Figure 6*c* shows that [Fe/H] $\sim$ 3 is required to roughly match the depth of the Fe II line blanketing. However, even in this case the fit is not very satisfying because, for example, the lines longward of 2300 Å are deeper in the data than in the model.

4.3. *Absorption Along the Line of Sight*

While the bare white dwarf model atmosphere analysis favors an enhanced Fe abundance, this is difficult to accept because we are aware of no circumstances under which nuclear synthesis could proceed to near completion in a white dwarf. New physics would be required. Furthermore, we note that absorption features in the *IUE* spectrum of the supergiant A2 star HD 197345 (Heck et al. 1984) are quite similar to those seen in our *HST* spectrum of OY Car's white dwarf, although the continuum of this star is much redder. Evidently circumstances similar to those in the extended atmosphere of an A2 supergiant give rise to an Fe II absorption spectrum quite similar to what we observe in OY Car.

We therefore consider sites outside the white dwarf atmosphere for the "iron curtain" (Shore 1992) that is veiling the white dwarf in OY Car. For example, the high 83° inclination may allow disk material to be present along lines of sight to the white dwarf.

To model the effects of intervening absorption, we assume that the computed synthetic spectrum of the white dwarf is further attenuated by absorption in a homogeneous slab of LTE gas, which is parameterized by the temperature T, electron density n_e, velocity dispersion ΔV, and hydrogen atom column density N_H. The solar composition is assumed. The velocity dispersion is introduced to account not only for a usual "microturbulent" velocity in the slab, but also for possible velocity gradients, which may be mimicked by turbulence (Shore & Aufdenberg 1993). The corresponding opacity of such a parameterized slab is calculated by a separate run of the program SYNSPEC. This means, in particular, that we use the

TABLE 2

BARE WHITE DWARF MODELS FITTED TO OPTICAL FLUXES

Model	$T_{\rm eff}$ (10^3 K)	log (*g*)	D^a (pc)	[He/H]	[Z/H]	[Fe/H]	Fit	χ^2/ν	ν
H.....	15.0	8.0	92	$-\infty$	$-\infty$	$-\infty$	UBR	1.17	4
S	15.2	8.0	91	0	0	0	UBR	0.92	4
Z1.....	15.0	8.0	91	0	1	0	UBR	0.91	4
Z2.....	14.2	8.0	93	0	2	0	UBR	0.91	4
Z3.....	13.7	8.0	114	0	3	0	UBR	0.91	4
FE3	14.9	8.0	94	0	0	3	UBR	0.89	4

[a] Distance assuming $R_W = 0.011 R_\odot$.

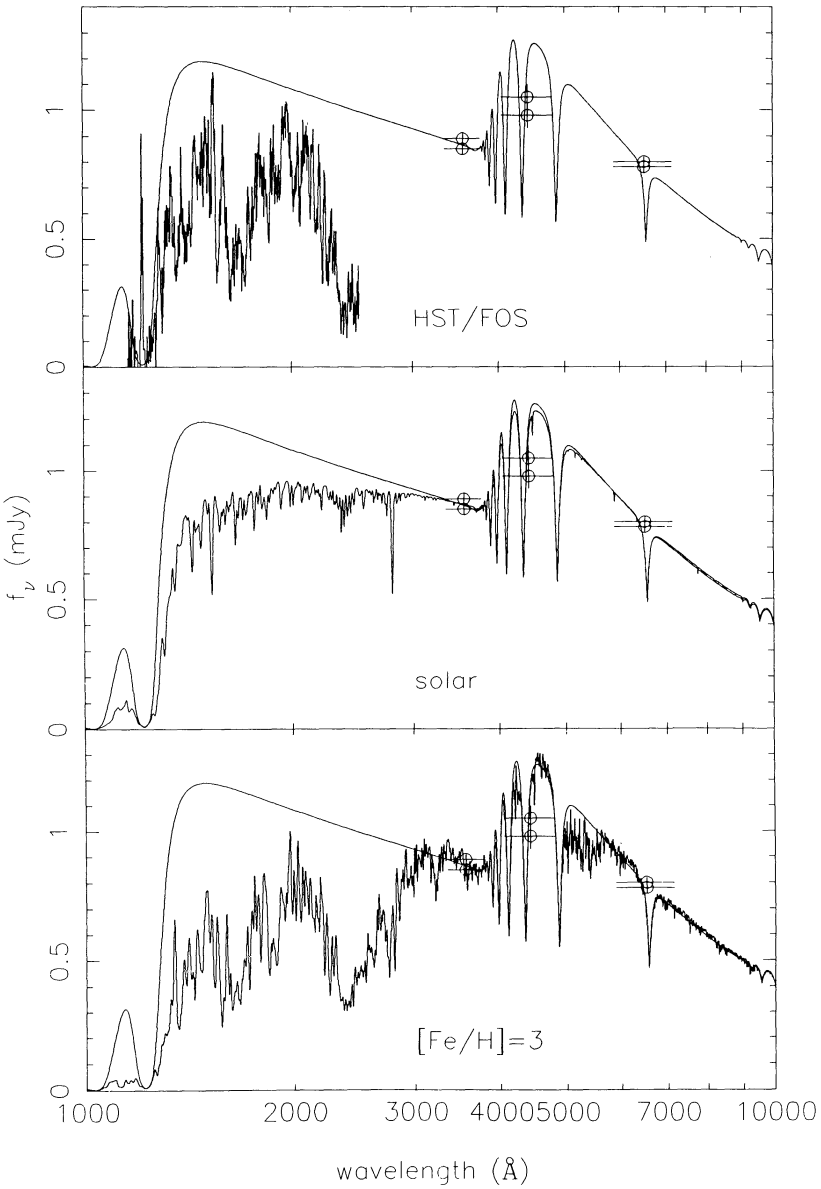

FIG. 6.—Model atmosphere spectra with $\log(g) = 8$, $T \sim 15 \times 10^3$ K, pure hydrogen (*a*) and solar (*b*) composition give a good fit to the optical fluxes of OY Car's white dwarf, but have insufficient line blanketing in the ultraviolet. A model with [Fe/H] = 3 gives a better fit (*c*).

same line list and the same source of damping parameters for lines as in a normal run of SYNSPEC (although, obviously, if the slab temperature is different from the white dwarf temperature, different lines contribute to the total opacity in the slab). Likewise, all the continuum opacity sources and electron scattering are taken into account in the slab. In our case, the name "iron curtain" is a misnomer, since *all* relevant opacity sources, including hydrogen lines and continua, and electron scattering, are taken into account. However, since most of the absorption features we see are due mainly to blended Fe II lines we will find it convenient to refer to this as an "Fe II curtain."

Assuming solar abundances, models with an LTE gas veiling the white dwarf have five parameters—the temperature T_W and solid angle $\pi(R_W/D)^2$ of the white dwarf, and the temperature T, electron density n_e, and thickness ΔR of the Fe II curtain. This model greatly improves the fit, but despite much exploration of the parameter space we still failed to find a reduced χ^2 below about 22. When we added the sixth parameter, the internal velocity dispersion ΔV, the reduced χ^2 immediately fell to around 4. At this point we attached the model to the Amoeba (Press et al. 1986) and proceeded to search for optimized model parameters.

Figure 7 exhibits our best-fit spectrum together with the *HST* data. This fit has $\chi^2/778 = 4.11$, where 778 is the number of data values. Residuals of the fit, shown along with the $\pm\sigma$ range in the lower panel of Figure 7, reveal several systematic features. Low residuals near 1400 Å are probably due to the Lα satellite line of quasi-molecular H I, which is not yet treated properly in the opacities of the model atmosphere code. High residuals near 1550 Å are probably due to residual C IV emission arising from close to the white dwarf. Somewhat large residuals of both signs are present shortward of 1230 Å, and here we suspect our error bars from the light curve decomposition may be underestimated. Elsewhere various absorption fea-

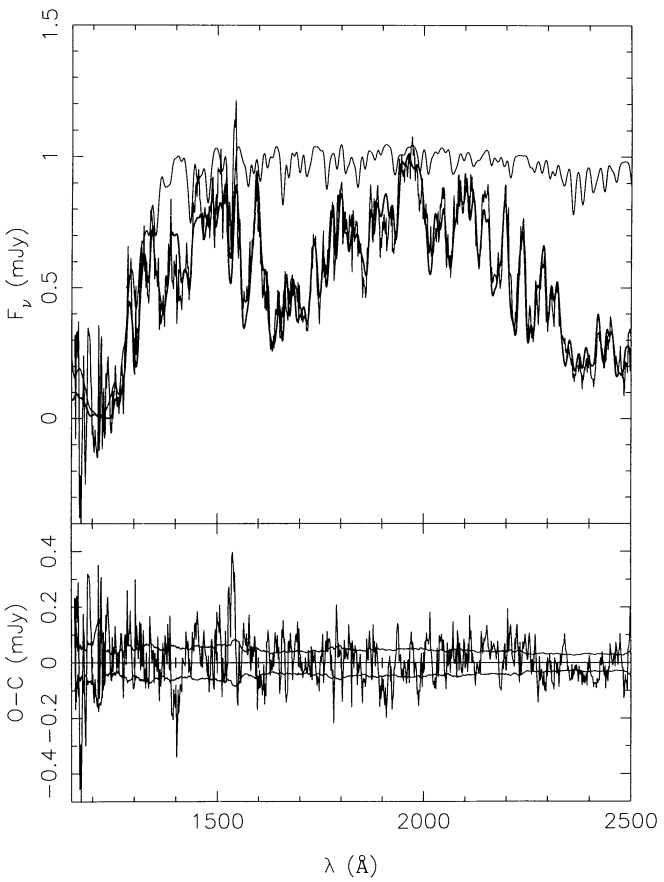

FIG. 7.—Top panel compares the *HST* spectrum of OY Car's white dwarf with the best-fit model of a solar-abundance white dwarf spectrum viewed through a solar-abundance LTE gas. Parameters of this model are summarized as Model 1 in Table 3. Most of the absorption features are due to Fe II. The unveiled white dwarf spectrum is also shown. Residuals are shown at the bottom along with the $\pm\sigma$ range of uncertainty in the data.

tures seen in the residuals probably represent real differences between the data and the simple model we are fitting. Despite these defects, we are nevertheless extremely pleased with the quality of this fit given the high density of information that it accounts for after fitting only six parameters.

All six parameters appear to be fairly well constrained by the data. We estimated 1 σ single-parameter confidence intervals by locating the extreme values of each parameter that satisfy $\chi^2 = \chi^2_{\rm min} + \Delta\chi^2$, where $\chi^2_{\rm min}$ is the global minimum value of the χ^2 statistic (Lampton, Margon, & Bowyer 1976). For $\Delta\chi^2$ the usual value is 1, but we adopt a larger value $\Delta\chi^2 = 4 \simeq \chi^2_{\rm min}/778$ to account for the large residuals. This is equivalent to increasing all of the error bars by a factor of $2 \simeq \sqrt{\chi^2_{\rm min}/778}$. Thus our formal error bars on the parameters may be somewhat conservative overestimates.

TABLE 3

VEILED WHITE DWARF MODELS FITTED TO THE *HST* SPECTRUM

	Model 1		Model 2	
Parameter	Value	$\pm\sigma$	Value	$\pm\sigma$
$T_{\rm W}$ (K)	16490	±200	16630	±300
D[a] (pc)	101	±2	100	±1
T (K)	9930	±210	8840	±150
$\log(n_e \cdot {\rm cm}^3)$	12.94	±0.40	12.64	±0.25
$\log(N_{\rm H} \cdot {\rm cm}^2)$	22.10	±0.10	22.19	±0.04
$\log(\Delta R/R_{\rm W})$	−0.07	±0.29	0.24	±0.09
ΔV (km s^{-1})	58	±2	0	
$R/R_{\rm W}$	∞		5.3	±0.9
$\chi^2/778$	4.11		3.65	

[a] Distance assuming $R_{\rm W} = 0.011 R_\odot$.

The best-fit parameter values and their estimated 1 σ uncertainties are summarized as Model 1 in Table 3. The white dwarf temperature is $T_{\rm W} \simeq 16{,}500$ K. Lowering (elevating) $T_{\rm W}$ produces a significantly wider (narrower) Lα absorption. The temperature of the veiling material, $T \simeq 10^4$ K, is constrained by the Fe II multiplet ratios, and by the ionization balance, which shifts to Fe I or Fe III at much lower or higher temperatures. The column density is fairly well constrained by the depths of the absorption features, and thus the density and path length are inversely correlated. We note that the 10^4 K temperature is similar but the 10^{13} cm^{-3} density of the veiling gas is rather higher than that typical of the solar chromosphere (5×10^{11} cm^{-3}). A lower density requires a lower temperature to keep Fe II, and this changes the relative strengths of the Fe II multiplets. The column density $N_{\rm H} \simeq 10^{22}$ cm^{-2} and velocity dispersion $\Delta V \simeq 60$ km s^{-1} are inversely correlated in order to maintain roughly correct depths and patterns of the absorption features.

The velocity dispersion is very important for the fit. The reduced $\chi^2/778$ drops from 22 for $\Delta V = 0$ to 4 for $\Delta V \simeq 60$. The velocity dispersion does not appreciably soften the spectral features, given our 9.2 Å resolution (1000–2000 km s^{-1}), but it does alter the pattern of the absorption by desaturating the stronger lines, increasing their equivalent widths relative to the weaker lines. Thus the 60 km s^{-1} velocity dispersion is accurately determined by the relative strengths of the absorption features even though it is much less than the instrumental resolution.

5. THE LOCATION OF THE VEILING GAS

The location of the absorbing gas that veils the white dwarf and the cause of its large internal velocity dispersion are somewhat uncertain. The absorption may occur in the upper atmosphere of the outer accretion disk (see, e.g., Smak 1992), where the lines of sight to the white dwarf inclined by $i = 83°$ from OY Car's rotation axis (Wood et al. 1989) pass over the disk plane at a height $z/R \sim 0.12$. In addition, lines of sight to the lower hemisphere of the white dwarf pierce the mid-plane of the inner disk, where absorption may occur unless this region is empty. We therefore consider it likely that the absorbing material is in some way associated with the disk.

5.1. *Shear-Curvature Broadening*

An important clue is the supersonic velocity dispersion $\Delta V \simeq 60$ km s^{-1}, which is Mach $\simeq 6$ for $T \sim 10^4$ K. Could so large a velocity dispersion be due to the Keplerian velocity field of the disk material? Of course there is no Doppler gradient along the line of sight to the exact center of the white dwarf because this line of sight passes through disk material that is moving exactly perpendicular to it. But lines of sight that are offset to the left (right) of the rotation axis pass through disk material moving with a small component of velocity toward (away from) us. Assuming a Keplerian velocity field, the Doppler shift is

$$V(x, R) = \left(\frac{x}{R_{\rm W}}\right)\left(\frac{R_{\rm W}}{R}\right)^{3/2}\left(\frac{GM_{\rm W}}{R_{\rm W}}\right)^{1/2} \sin i\,, \qquad (3)$$

where x is the minimum distance between the line of sight and the rotation axis, and R is the distance from the white dwarf, whose mass is M_W and radius R_W. Distributing gas along the line of sight with a dispersion ΔR about a mean radius R gives rise to a Doppler gradient along the line of sight that mimics a turbulent broadening with a velocity dispersion

$$\Delta V(x, R) = \frac{\partial V(x, R)}{\partial R}\,\Delta R = \frac{3}{2}\left(\frac{x}{R_W}\right)\left(\frac{\Delta R}{R}\right)\left(\frac{R}{R_W}\right)^{-3/2}\left(\frac{GM_W}{R_W}\right)^{1/2}\sin i\,. \quad (4)$$

This expression is valid for $\Delta R/R \lesssim 1$. We call this effect "shear-curvature" broadening because it requires both properties of the Keplerian velocity field, shear in the radial direction and curvature of streamlines in the azimuthal direction.

To model the effect of shear-curvature broadening, we divide the projected area of the white dwarf into about 10 strips for different values of x ranging from $-R_W$ to $+R_W$. We then use SYNSPEC to calculate the spectrum for each strip, and include veiling with a Doppler shift V and velocity dispersion ΔV appropriate for each strip from the formulae above, and then we sum the contributions weighted by the appropriate area for each strip. We ignore limb-darkening, white dwarf rotation, and internal turbulent broadening.

The six parameters of this new model are T_W, D, T, n_e, R, and ΔR. The hydrogen column density is now a dependent parameter $N_H = n_H(T, n_e)\Delta R$. The best-fit parameters for this case are summarized as Model 2 in Table 3. The values of T_W and D are essentially the same as before, while T and n_e are both somewhat lower (maintaining the same ionization balance). Because the velocity dispersions are proportional to $R^{-5/2}\Delta R$, R, and ΔR are highly correlated parameters satisfying $\Delta R/R \simeq (R/12R_W)^{1.5}$.

The best-fit model distributes the gas at $R/R_W \simeq 5$ with a radial dispersion $\Delta R/R \simeq 0.3$. What selects this radius? The gas cannot be at a much smaller R because the Doppler broadening, of order ± 400 km s$^{-1}(R_W/4.5R)^{3/2}$, then becomes so large that the model's absorption features are wider than those in the data. At much larger radii, $R > 12R_W$, we require $\Delta R/R > 1$ to make $\Delta V \simeq 60$ km s^{-1}, and the increased path length at roughly constant column density drives the density down so far that Fe II becomes Fe III and can no longer fit the shape of the absorption spectrum. Thus if shear-curvature broadening is the sole source of the velocity dispersion, then the absorbing gas must be at $R/R_W \simeq 5$, well inside the outer rim of the disk ($R_D/R_W \sim 25.5$; Table 1).

5.2. *Absorption in the Inner Disk?*

We consider here whether the absorbing gas could be located near the mid-plane of the inner disk (e.g., Smak 1992). In this case we would expect to have a relatively unobstructed view of the upper hemisphere of the white dwarf, but we would view the lower hemisphere of the white dwarf through the plane of the inner disk. The line of sight to the lowest point on the projected white dwarf pierces the disk plane at a radius $R/R_W = \sec i \simeq 8$. The best-fit value $R/R_W \simeq 5$ needed to make shear-curvature broadening match the observed velocity dispersion seems quite compatible. To test this possibility further, we considered a model in which a fraction $(1 + \cos i)/2$ of the white dwarf surface is viewed without obscuration and the complementary fraction $(1 - \cos i)/2$ is viewed through the Fe II curtain. After optimizing the parameters, the best-fit model had a $\chi^2/778 \simeq 12$. This poor fit arises because the inner disk obscures just under half of the white dwarf surface, thus the absorption features cannot go lower than about half of the unobscured white dwarf flux. But the observed absorption features around 1600–1700 Å and 2300–2500 Å go deeper, showing that the Fe II curtain veils at least $\sim 80\%$ of the white dwarf. This makes it unlikely that the Fe II curtain is located in the inner disk unless its vertical thickness is of order R_W.

5.3. *Supersonic but Sub-Keplerian Disturbances in the Outer Disk*

If the disk surface has a concave shape, then the most natural place to find absorbing material is where the line of sight skims over the disk's outer rim at $R_D \simeq 25R_W$. If we place the absorbing material here, then shear-curvature broadening cannot account for the supersonic velocity dispersion since that would require $\Delta R/R \sim 3$. The large velocity dispersion may then be interpreted literally as Mach $\simeq 6$ Doppler gradients over a distance ΔR in the radial direction. Compared with the Keplerian flow, the supersonic velocity dispersion is $\Delta V/V_{Kep} \simeq 0.07(R/R_D)^{1/2}$. This supersonic but sub-Keplerian disturbance is unlikely to take the form of small-scale turbulence, because such flows would quickly dissipate in shocks. But larger scale disturbances of the velocity field near the rim of the disk, perhaps driven by interaction with the gas stream, might persist for some time since the timescale for reestablishing hydrostatic equilibrium is of the same order as the Kepler orbit time.

For comparison purposes, let's consider briefly an isothermal treatment of the vertical disk structure assuming hydrostatic equilibrium. This gives a Gaussian density distribution

$$\rho(z) = \rho_0\, e^{-(z/\Delta z)^2/2}\,, \quad (5)$$

with a vertical dispersion

$$\frac{\Delta z}{R} = \frac{C_s}{V_{Kep}} = \left(\frac{\gamma kTR}{\mu m_H GM_W}\right)^{1/2} \simeq 0.012\left(\frac{R}{R_D}\right)^{1/2}, \quad (6)$$

where $T \simeq 10^4$ K is the measured gas temperature, γ is the ratio of specific heats, μ is the mean molecular weight, and m_H is the mass of the hydrogen atom. Our fit to the absorption spectrum measures the density of the absorbing gas at a height of $(R \cos i)/\Delta z \simeq 10(R/R_D)^{-1/2}$ standard deviations above the mid-plane of the Gaussian disk:

$$\rho(z = R\cos i) = \frac{\mu N_H m_H}{2\Delta R} \simeq 3 \times 10^{-11}\ \text{g cm}^{-3}\,. \quad (7)$$

From this we can infer a vertically integrated surface density of

$$\Sigma = 2\rho_0\,\Delta z = \mu m_H N_H \frac{\Delta z}{\Delta R}\, e^{(R\cos i/\Delta z)^2/2} \simeq 10^{-3}\ \text{g cm}^{-2}\left(\frac{R}{R_D}\right)^{1/2}\left(\frac{R}{5\Delta R}\right)e^{50(R/R_D)}\,, \quad (8)$$

and the mass of the disk annulus is then

$$M_{ring} = 2\pi R\,\Delta R\Sigma = 2\pi R\,\Delta z \mu m_H N_H e^{(R\cos i/\Delta z)^2/2} \simeq 10^{18}\ \text{g}\left(\frac{R}{R_D}\right)^{3/2} e^{50(R/R_D)}\,. \quad (9)$$

For $R \sim R_D$, these estimates of Σ and M_{ring} are implausibly large because of the enormous exponential factor that is needed to correct for the density being measured 10 Gaussian widths above the disk's mid-plane. Without this large exponen-

tial factor, the surface density and mass are more reasonable. We conclude that thermal pressure in the outer disk cannot elevate this much gas up to $z = 0.12R$, and that the disk thickness Δz must therefore be much larger than the hydrostatic equilibrium value given by equation (6).

What holds the absorbing material up above the disk plane at a height $z/R = \cos i = 0.12$? We clearly need some nonthermal mechanism of vertical support. Magnetic pressure could in principle support the gas, as in a solar prominence, but this requires $B^2/8\pi \sim GM_W z^2/R^3 = \rho V_{Kep}^2 \cos^2 i$, or $B \simeq 10^6 (R/R_D)^{1/2}$ G, which is unrealistically large for the disk. A natural alternative is the internal motions themselves. If the velocity dispersion in the vertical direction is similar to the Mach $\simeq 6$ velocity dispersion observed in the radial direction, that would be sufficient to boost material up to the required height. Thus a model in which the outer disk is supported vertically by supersonic (Mach $\simeq 6$) but sub-Keplerian velocity disturbances appears to be consistent with the data.

Figure 8 shows our prediction for the spectrum of OY Car's white dwarf extending from the ultraviolet into the optical and near-infrared regime. The ratio of the two spectra, shown in the bottom panel of Figure 8, is roughly $e^{-\tau(\lambda)}$, where $\tau(\lambda)$ is the optical depth of the absorbing gas. Note the characteristic pattern of Fe II line blanketing, depressing the ultraviolet light most deeply around 2500 and 1600 Å. A similar pattern of absorption features is seen in *IUE* spectrum of the quiescent dwarf nova HT Cas (Wood, Horne, & Vennes 1992), and may be due to a similar mechanism. This absorption may be important in shaping the ultraviolet spectra of all high-inclination cataclysmic variables. The optical and near-infrared regions are relatively free of Fe II absorption features, which may explain why this absorbing gas was not clearly recognized in earlier optical studies.

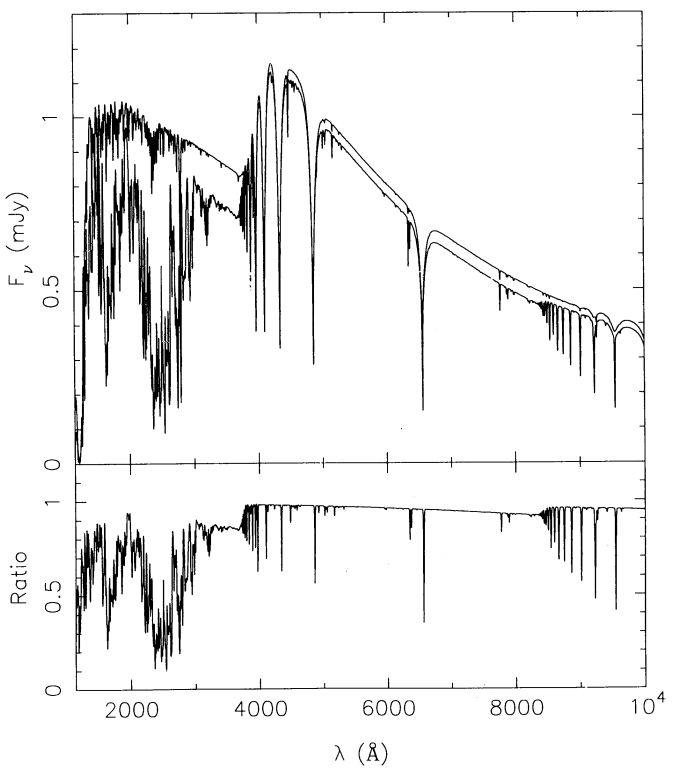

FIG. 8.—Top panel shows at 9.2 Å resolution the predicted ultraviolet, optical, and near-infrared spectrum of OY Car's white dwarf based on the fit to the 1150–2500 Å *HST* data shown in Fig. 7. The theoretical white dwarf spectrum is shown both before and after it passes through the absorbing medium that we believe is located near the outer rim of the accretion disk. The lower panel showing the ratio of the two spectra indicates that the absorbing gas produces a characteristic pattern of Fe II line blanketing with deep features around 1600 and 2500 Å, modest optical depths in the Balmer and Paschen continua, and deep absorptions in the cores of Balmer and Paschen lines.

The absorbing gas has hydrogen bound-free and bound-bound opacities which produce observable effects in the optical and near-infrared. The optical depths reach 0.12 and 0.07 in the Balmer and Paschen continua, respectively, deepening the white dwarf's Balmer jump in absorption at 3650 Å, and cutting a small Paschen jump near 8200 Å. The bound-bound opacity drills deep and narrow absorptions into the cores of the white dwarf's Stark-broadened Balmer and Paschen lines. If the absorbing gas is distributed in azimuth around the rim of the disk, the significant optical depths in the Balmer lines and continua and the relatively large area of order $2\pi R \Delta R$ imply that the same 10^4 K gas that we see as Fe II absorption in the ultraviolet must also produce a strong Balmer jump and Balmer emission lines similar to those seen in optical spectra of OY Car and many other quiescent dwarf novae. It would be interesting to build a model disk chromosphere with temperature, surface density, and velocity dispersion parameterized as functions of radius in the disk to see if such a model can fit simultaneously the Balmer emission lines and Fe II absorption lines. This important step toward understanding the structure of quiescent accretion disks, is beyond the scope of the present investigation, but should be a goal for future work.

The widths of the two peaks in the velocity profile of the Balmer emission lines from the quiescent disk can be used to estimate the azimuthal velocity dispersion, provided the disk is assumed to have a sharp outer edge. Modeling of the Hβ emission line from the disk in the dwarf nova U Gem yields $V_{turb} \sim 0.12 V_{Kep}$ for the azimuthal velocity dispersion in the outer disk (Stover 1981). This is similar to the velocity dispersion we have measured from the Fe II absorption in OY Car, and suggests that supersonic disturbances are common in the outer regions of quiescent disks.

The Fe II curtain effect along the line of sight to the bright central white dwarfs in quiescent dwarf novae probably offers us a relatively clean absorption-line probe of the Balmer emission-line region in the outer disk. It would be interesting to observe the Fe II lines at somewhat higher resolution to measure the mean velocity, velocity dispersion, temperature, and column density of the absorbing gas as a function of binary phase, for that could be used to determine how the radial velocity (hence radius), radial velocity dispersion (or velocity gradient), and column density (hence vertical disk thickness) vary with azimuth around the rim of the disk. Such detailed kinematic information could establish whether the gas stream is driving the supersonic velocity disturbances, and would provide an observational basis for studying dynamics in the outer disk, for example the process by which vertical hydrostatic equilibrium is established, the nature of tidal distortions produced by the companion star at different disk radii, and the decay of the elliptical disk distortion (Hessman et al. 1992) at the end of a superoutburst.

6. CONCLUSIONS

We have used the *HST*'s Faint Object Spectrograph to acquire ultraviolet spectra covering 1150–2500 Å with 9.2 Å spectral and 9.5 s time resolution during an eclipse of the dwarf

nova OY Car in its quiescent state. Analysis of the eclipse permits us to isolate separate spectra for the white dwarf, accretion disk, and bright spot. Our principal findings may be summarized as follows:

1. The white dwarf dominates the ultraviolet spectrum. Its spectrum has a broad Lα absorption and an unexpected forest of blended Fe II absorption lines that we attribute to absorption by circumstellar material, probably in the disk. We can fit the spectrum using a solar-abundance white dwarf with $\log g = 8$ and $T_W \simeq 16.5 \times 10^3$ K veiled by a solar-abundance LTE gas with $T \simeq 10^4$ K, $n_e \simeq 10^{13}$ cm^{-3}, $N_H \simeq 10^{22}$ cm^{-2}, and velocity dispersion $\Delta V \simeq 60$ km s^{-1}.

2. The supersonic (Mach $\simeq 6$) velocity dispersion is required for a good fit because it controls ratios of highly saturated to weakly saturated absorption features. The velocity dispersion may be attributed to the disk's Keplerian velocity field if the absorbing gas is distributed with $\Delta R/R = (R/12R_W)^{3/2}$. The best-fit model distributes this gas in the inner accretion disk with $R/R_W \simeq 5$ and $\Delta R/R \simeq 0.3$. This suggests that we are simply viewing the lower hemisphere of the white dwarf through the mid-plane of the inner disk at an angle sec $i \sim 8$. However, this inner-disk model leaves the upper hemisphere of the white dwarf in clear view, whereas several of the observed absorption features are over 80% deep.

3. We can place the veiling gas near the outer rim of the disk, as seems likely for a concave disk surface, but this region must then have supersonic (Mach $\simeq 6$) but sub-Keplerian ($\Delta V/V_{Kep} \sim 0.07$) velocity disturbances in order to account for the observed velocity dispersion in the radial direction, and to produce vertical motions sufficient to elevate gas above the disk plane to $z/R = \cos i = 0.12$. If the vertical dispersion of the disk is $\Delta Z/R \sim 0.12$, we can estimate the surface density and mass of the ring of absorbing material as $\Sigma \simeq 10^{-3}$ g cm^{-2} $(R/5\,\Delta R)(R/R_D)^{1/2}$ and $M_{ring} \simeq 10^{-18}\, M_\odot (R/R_D)^{1/2}$. The velocity disturbances might be driven by the impact of the gas stream, since a disturbed disk would require several Kepler periods to reestablish a hydrostatic equilibrium structure. The same 10^4 K gas that we see as Fe II absorption in the ultraviolet has sufficient optical depth to produce Balmer continuum and line emission similar to that seen in the optical spectra of OY Car and other quiescent dwarf novae.

4. The eclipse indicates that the quiescent accretion disk is quite faint in the ultraviolet, its intensity being less than 1/30 that of the white dwarf. The outer disk produces a residual flux at mid-eclipse that rises smoothly longward of 2000 Å. The radial intensity profile at these wavelengths can be described roughly as R^b with $b = +0.2 \pm 0.5$.

5. The bright spot at the rim of the disk is also faint in the ultraviolet, though its contribution exceeds that of the disk at wavelengths shortward of 2000 Å. The bright spot egress feature indicates a disk radius $R_D/a \sim 0.37$.

6. The C IV λ1549 emission displays a broad eclipse with a fractional depth of about 0.5. Its flux and radial velocity are significantly different before and after eclipse, but the accuracy of the data is not sufficient to determine from the behavior of the line during the eclipse whether this line arises from the Keplerian disk or from a wind originating near the white dwarf. Weak permitted emission lines of C II, Si II, Si III, Si IV, and Al III are detected at mid-eclipse, while N V and He II are not.

7. We see fast flares lasting about 1 minute with broad-band spectra rising into the UV. The distribution of phases at which these flares occur shows that they do not arise in the bright spot, and most likely they arise from very close to the white dwarf. (Spacecraft jitter is ruled out.)

We are currently modeling eclipses of OY Car obtained with *HST* at several epochs in the quiescent period following a superoutburst. This should yield a history of the white dwarf temperature and the properties of the veiling gas as the system relaxes from the intense heating experienced during the superoutburst.

We thank Steve Shore for useful discussions, Ed Sion and Richard Wade for thoughtful comments on the manuscript, and Melvin Hoare for assistance in accessing the *IUE* archives. K. H. enjoyed hospitality at the Astrophysics Department of Oxford University, and at the Institute of Astronomy and Royal Greenwich Observatory in Cambridge. Support for this work was provided by NASA through grant GO-2380 from the Space Telescope Science Institute, which is operated by the Association of Universities for Research in Astronomy, Inc., under NASA contract NAS5-26555. This research was also sponsored by NASA's Long Term Space Astrophysics Research Program through grant NAGW-2678, and by the STScI Visitors Program.

REFERENCES

Heck, A., Egret, D., Jaschek, M., & Jaschek, C. 1984, *IUE* Low-Dispersion Spectra Reference Atlas Part 1. Normal Stars (ESA SP-1052)
Hessman, F. V., Mantel, K.-H., Barwig, H., & Schoembs, R. 1992, A&A, 263, 147
Horne, K., & Eracleous, M. 1993, CAL/FOS Instrument Science Report 091 (Baltimore: STScI)
Horne, K., & Saar, S. H. 1991, ApJ, 374, L55
Hubeny, I. 1988, Comp. Phys. Comm., 52, 103
———. 1994, TLUSTY and SYNSPEC: A User's Guide, in press
Hubeny, I., Hummer, D. G., & Lanz, T. 1994, A&A, in press
Hubeny, I., & Lanz, T. 1992, A&A, 262, 501
Hummer, D. G., & Rybicki, G. B. 1982, ApJ, 254, 767
Kinney, A. 1992, *Hubble Space Telescope* Faint Object Spectrograph Instrument Handbook, Version 2.0 (Baltimore: STScI)
Kurucz, R. L. 1990, in Trans. IAU, 20B, 168
Lampton, M., Margon, B., & Bowyer, S. 1976, ApJ, 208, 177
Lanz, T., Hubeny, I., Cheng, F.-H., & Horne, K. 1992, BAAS, 24, 1203
Press, W. H., Flannery, B. P., Teukolsky, S. A., & Vetterling, W. T. 1986, Numerical Recipes (Cambridge: Cambridge Univ. Press)
Schoembs, R., Drier, H., & Barwig, H. 1987, A&A, 50
Shore, S. N. 1992, in ASP Conf. Ser. 22, Nonisotropic and Variable Outflows from Stars, ed. L. Drissen, C. Leitherer, & A. Nota (San Francisco: ASP), 342
Shore, S. N., & Aufdenberg, J. P. 1993, ApJ, 416, 355
Smak, J. 1992, Acta Astron., 42, 323
Stover, R. J. 1981, ApJ, 248, 684
Wood, J. H., & Horne, K. 1990, MNRAS, 242, 606
Wood, J. H., Horne, K., Berriman, G., & Wade, R. 1989, ApJ, 341, 974
Wood, J. H., Horne, K., & Vennes, S. 1992, ApJ, 385, 294
Wood, J. H., Irwin, M. J., & Pringle, J. E. 1985, MNRAS, 214, 475